Dynamic Modeling of Suspension Crystallizers, Using Experimental Data

Rob A. Eek, Sjoerd Dijkstra, and Gerda M. van Rosmalen
Mechanical Engineering Systems and Control Group, Delft University of Technology, Mekelweg 2, 2628 CD Delft, The Netherlands

A model for the dynamics of a single-stage suspension crystallizer is developed, which serves as a basis for process analysis and the design of controllers. A population balance for the dynamics of the crystal size distribution (CSD) with mass and heat balances is described, as well as empirical relations for the separation efficiency of classified particle removal systems, the initial CSD, and the crystallization kinetics. A continuous pilot crystallizer is used that is equipped with a separator and dissolver for fine crystals and a CSD sensor based on forward light scattering. The process and sensor are modeled separately. The sensor model is based on Fraunhofer light scattering theory assuming rectangular-shaped particles. CSD dynamics data are obtained from startup experiments with the pilot plant at different process conditions. Experimental process data show a strong effect of fines and the slurry retention time on the CSD dynamics. A nonlinear parameter estimation procedure determines the empirical parameters directly from raw sensor data. The model fits accurately to the measured data. Evidence is found for the existence of a population of slow growing crystals with a growth rate approximately ten times lower than the fast growing crystals. A strong correlation is found between the total surface area of crystals with a size larger than 600 μm and the nucleation rate.

Introduction

Crystallization from solution is an important industrial separation and purification process in which a crystalline solid phase is formed from a multicomponent liquid solution. Crystallization processes are particulate processes generating a spectrum of differently sized particles, characterized by the crystal size distribution (CSD).

The CSD of crystals produced by continuous industrial crystallizers is often poorly shaped due to badly dampened or oscillatory behavior of the CSD in time. In industrial practice this behavior limits the product quality and puts constraints on the performance of downstream crystal handling processes, for example, thickeners, centrifuges, and dryers. To suppress this undesired dynamic behavior, CSD control systems are demanded. In general the design of effective controllers requires a set of sufficiently effective process inputs (actuators), robust sensors that should provide sufficient information on the dynamics to be controlled, as well as a process model describing the relevant dynamics.

Modeling the dynamic behavior of an industrial crystallizer requires knowledge of several complex crystallization phenomena, like crystal birth (nucleation), crystal growth, and breakage or abrasion (attrition) phenomena caused by particle-particle or particle-crystallizer interactions (Randolph and Larson, 1988). These phenomena depend on the physical properties of the substance system, the process operating conditions, and hydrodynamic phenomena that depend on the geometry and scale of the reactor.

First-principle models include several unknown parameters related to empirical relations for hydrodynamics and crystallization kinetics. These parameters have to be estimated from experimental data by a numerical model optimization procedure. Published data deal largely with the estimation of crystallization kinetics for idealized stationary MSMPR reactors based on stationary CSD data. The applicability of this approach is limited since a large class of crystallizers exhibit

Correspondence concerning this article should be addressed to G. M. van Rosmalen. Current address of G. M. van Rosmalen: Laboratory for Process Equipment, Delft University of Technology, Leeghwaterstraat 44, 2628 CA Delft, The Netherlands.

Current address of R. A. Eek: Bayer AG, ZF-TST, Bldg. E41, D-51368, Leverkusen, Germany.

nonstationary behavior caused by disturbances or intrinsic open-loop instabilities. Only a few examples are present on model optimization with dynamic CSD data. Tavare and Garside (1986) describe an approach which uses a transient CSD response from a batch crystallizer. Rawlings et al. (1993) address the problem of parameter and parameter confidence interval estimation from dynamic data. In most contributions the main limitation is the absence of accurate and robust online measurement systems that provide sufficiently informative data on the kinetics to be estimated.

This article addresses the problem of model development for the CSD dynamics in a suspension crystallizer, using experimental (pilot) process data. The aims of this study are as follows:

1. To combine knowledge on particulate phenomena (particle size and shape, CSD sensing, and size classification) with crystallization phenomena (crystal nucleation and growth kinetics and the attrition of particles) to obtain a parameterized model that can be used to model larger-scale industrial reactors.
2. To measure the effect of different process input parameters on the CSD dynamics of a pilot-scale crystallizer and utilize the resulting experimental data sets to estimate unknown parameters in this model.

A general dynamic model for a single-stage suspension crystallizer including CSD actuators and sensors will be presented. The reduction of this model to a set of simplified equations is presented for a continuous constant volume isothermal evaporative crystallizer that is also used as a data-generating system for the experimental work described here. Experimental data obtained from the startup response of the 970-L experimental DTB crystallizer are presented for different values of process input parameters. A numerical parameter estimation procedure is followed, which leads to a set of optimal parameter values. Based on these estimated parameter values, conclusions are drawn with respect to the physical phenomena that govern the dynamic behavior of the pilot crystallizer. All experimental results are derived for the ammonium sulfate-water system.

Process Modeling

The crystallizer studied here is a single-stage suspension crystallizer equipped with classified fines and product removal systems and a fines dissolver. The system boundary and the set of process input and output variables together with some major process parameters are summarized in Figure 1. We assume that fines are totally dissolved by heating (P_{ex}). For cooling crystallizers ($Q_v = 0$) the heat input (P_{in}) will attain a negative sign. When product is removed without classification ($Q_{pf} = Q_p$), the product retention time (mean residence time) is defined as $r_p = V/Q_p$, with V the crystallizer volume.

Characterization of particles

The CSD is characterized by the population density function $n(x, t)$, defined by

$$n(x, t) \triangleq \lim_{\Delta x \to 0} \frac{\Delta N(x, t)}{\Delta x}, \tag{1}$$

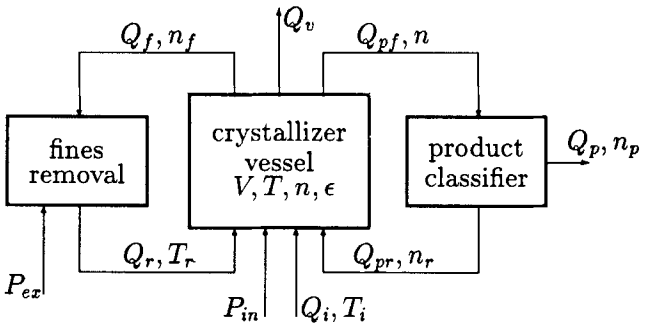

Figure 1. Suspension crystallizer, equipped with a fines and product removal system.

with $N(x, t)$ the cumulative number function describing the number of crystals per unit volume, with a size equal to or lower than x.

Individual crystals are physically characterized by their size and shape. Particles are considered to have a rectangular shape with dimension $x_l \cdot x_w \cdot x_w$ and have an (average) aspect ratio α. The latter is defined by $\alpha = x_l/x_w$ and can be estimated from visual inspection of the particles. In our model we defined the crystal size x to be the size x_l. The corresponding crystal shape factor, defined by the ratio of the particle volume v and the cube of a particle with size x: $k_v = v/x^3$, is then given by $k_v = 1/\alpha^2$. This factor is used in the mass balances to correct for a possible noncubic shape of the particles.

As will be discussed below, a sensor model is developed for rectangular-shaped particles with the same aspect ratio. With respect to particle size and shape a consistent basis is thus created for the comparison of modeled and measured CSD dynamics.

Modeling size classification

The size classification subsystem for the fines and product removal loops is schematically depicted in Figure 2. An input flow Q_0 containing crystals with a population density n_0 is separated into two different flows Q_1 and Q_2, each containing crystals with a population density of n_1 and n_2, respectively. The flow Q_2 is removed from the process and the flow Q_1 is returned to the crystallizer.

To model size classification in the fines and product removal system the following assumptions are made: the saturation condition of the liquid containing the crystals to be separated is unaltered, that is, the system is isothermal and no growth or dissolution of crystals occurs; no breakage or attrition of particles occurs; and dynamics or holdup time in the separator is neglected.

The general separator model constrained with the given assumptions is described by two mass balances, for example, a solid- and liquid-phase balance:

$$Q_2(t)[1 - \epsilon_2(t)] = Q_0(t)[1 - \epsilon_0(t)] - Q_1(t)[1 - \epsilon_1(t)], \tag{2}$$

$$Q_2(t)\epsilon_2(t) = Q_0(t)\epsilon_0(t) - Q_1(t)\epsilon_1(t), \tag{3}$$

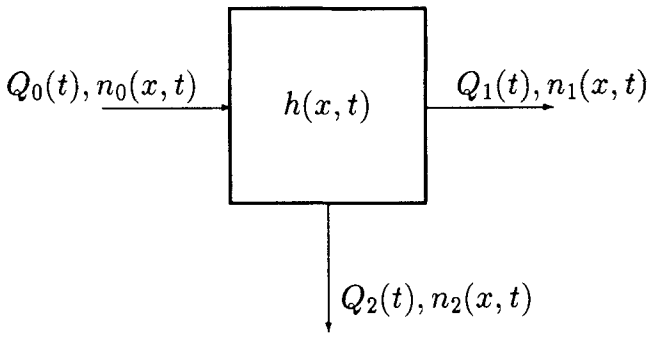

Figure 2. Particle size classifier.

and the number balances for, respectively, the returned and removed flow:

$$[1-h(x,t)]Q_0(t)n_0(x,t)=Q_1(t)n_1(x,t) \tag{4}$$

$$h(x,t)Q_0(t)n_0(x,t)=Q_2(t)n_2(x,t). \tag{5}$$

The function $h(x, t)$ is the removal efficiency function that describes the probability that a particle with size x is removed from the crystallizer volume and ϵ is a void fraction calculated from

$$\epsilon_*(t)=1-k_v\int_0^\infty n_*(x,t)x^3\,dx=1-k_v m_{3*}(t), \tag{6}$$

with m_{3*} the third moment of the population density n_* in a certain flow $(*)$.

Fines classification. The fines removal system includes a fines classifier and a fines dissolver. Fines classification can be achieved in an annular zone based on differences in settling velocities of crystals. According to Eq. 5 the fines distribution $n_f(x, t)$ can be described as

$$n_f(x,t)=\frac{Q_{ff}(t)}{Q_f(t)}h_f(x,t)n(x,t), \tag{7}$$

with $h_f(x, t)$ the fines removal efficiency, $Q_f(t)$ the fines removal flow, and $Q_{ff}(t)$ the unclassified flow that enters the bottom section of the annular zone.

The factor $Q_{ff}(t)/Q_f(t)$ is a flowsplit factor denoted here as γ_f. Assuming that only particles and no liquid returns from the annular zone back to the main crystallizer volume, the flowsplit factor can be calculated from $\gamma_f(t)=\epsilon_f(t)/\epsilon(t)$, with ϵ and ϵ_f the void fractions of the fines slurry flow and the slurry in the crystallizer, respectively. In the literature this factor is often taken to equal 1, which is a good approximation when the void fraction in the crystallizer is high. Note that for industrial plants that mostly operate at 10–30% solids this approximation causes a significant error.

In the literature several empirical relations are presented for the function $h_f(x, t)$. Randolph and Larson (1988), Koskinen and Norden (1981), and de Leer (1976) discuss different idealized functions that describe constant classification behavior. Randolph and Larson present the so-called $R-Z$ model, which is a combined model, to describe both classified fines and product removal. Experimental results (de Leer et al., 1976; Koskinen and Norden, 1981) make clear that ideal classification of fines will not occur. Cut-size calculations may deviate from measured values because of the asphericity of crystals and hindered settling or flotation due to air bubbles occurring in the fines trap. The nonideal sharpness of the actual efficiency curve may result from hydrodynamic effects in the classifying section. Furthermore, classifying conditions can change with varying fines removal flows. The following nonlinear two-parameter function is proposed to describe the fines removal efficiency:

$$h_f(x,t)=\frac{1}{1+\left(\dfrac{x}{x_c(t)}\right)^{p_{f2}}}. \tag{8}$$

Because the solid concentration in the fines loop is low (< 1 percent), the cut-size $x_c(t)$, defined as the crystal length where the probability of withdrawal from the crystallizer volume is 50 percent, can be derived from Stokes' relation for calculating settling velocities:

$$x_c(t)=\sqrt{p_{f1}Q_f(t)}. \tag{9}$$

The constant factor p_{f1} can be calculated (for spheres) from

$$p_{f1}=\frac{18\mu}{A\Delta\rho g}, \tag{10}$$

with μ is the absolute viscosity of the mother liquor, $\Delta\rho$ the density difference between particles and liquid, A the cross-sectional area of the classifier, and g the gravity constant. In the model, however, p_{f1} is taken as an unknown parameter since the value calculated from Eq. 10 is biased by the asphericity of the particles and hindered settling effects. As depicted in Figure 3, with Eq. 8, an S-shaped curve is obtained with a point of inflection given by the cutsize and a degree of imperfection given by parameter p_{f2}.

The separated fines are dissolved by heating the fines slurry flow. To model fines dissolution we assume that all fines dissolve. With this assumption two mass balances and a heat

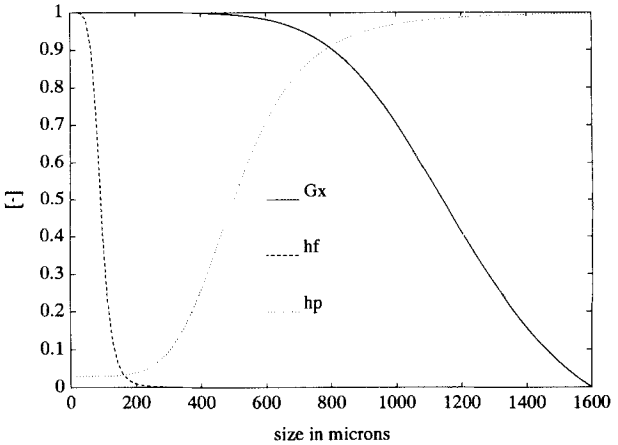

Figure 3. Examples of classification functions h_f and h_p and the growth function G_x.

balance over the fines section are derived. The corresponding equations are summarized in the Appendix.

Product classification. Product classification can be established with mechanical separators, for example, vibrating screens; gravitational separators, for example, hydraulic classifiers; and centrifugal separators, for example, hydrocyclones. For these systems the product distribution n_p can be calculated, analogous to the fines removal function, from

$$n_p(x, t) = \frac{Q_{pf}(t)}{Q_p(t)} h_p(x, t) n(x, t), \tag{11}$$

where Q_p is the product flow, Q_{pf} the unclassified flow from the crystallizer, and $n(x, t)$ the population density of crystals in the crystallizer. The corresponding product flowsplit factor is now defined by

$$\frac{Q_{pf}(t)}{Q_p(t)} = \gamma_p = \frac{\epsilon_r(t) - \epsilon_p(t)}{\epsilon_r(t) - \epsilon_{pf}(t)}, \tag{12}$$

with ϵ_r, ϵ_p, and ϵ_{pf} the void fractions of the return flow, the product flow, and the classifier feed flow, respectively. These void fractions are calculated from Eq. 6. A general model for classification is used to describe product classification:

$$h_p(x) = \frac{p_{p3} + (1 - 2p_{p3}) \left(\frac{x}{p_{p1}} \right)^{p_{p2}}}{1 + (1 - 2p_{p3}) \left(\frac{x}{p_{p1}} \right)^{p_{p2}}}. \tag{13}$$

This function is parametrized with three parameters: the cut-size p_{p1}, the imperfection p_{p2}, and an offset p_{p3}. The latter p_{p3} defines the void fraction, leaving the crystallizer with the separated product. An example of this product classification function is given in Figure 3. A comprehensive overview on modeling of solid-liquid separators is given by Svarovsky (1990). The product flow leaving the product classification system can now be calculated from

$$Q_p(t) = Q_{pf}(t) \epsilon_{pf}(t) p_{p3} + k_v \int_0^\infty h_p(x) n(x, t) x^3 \, dx. \tag{14}$$

The total set of parameters related to fines and product classification is denoted as

$$\theta_C = \{\{p_{f1}, p_{f2}\}, \{p_{p1}, p_{p2}, p_{p3}\}\}. \tag{15}$$

Modeling crystallization phenomena

Hydrodynamics. In the first instance it is assumed that the crystallizer volume is ideally mixed. Spatial segregation of particles, however, will occur. Both Jager (1990) and Hallas and Hannan (1990) present some preliminary results of a mixing study in a 1-m^3 DTB crystallizer equipped with a marine-type impeller. Both estimated the circulation speed of slurry at 300 rpm impeller speed to be 350 mm/s. Experimental results of Koskinen and Norden (1981) show that the settling velocity of ammonium sulphate crystals decreases for larger void fractions. A velocity of 7.5 mm/s was found for crystals with a size of 400 μm and a void fraction of 80%. Therefore, larger crystals with a size $x > 500$ μm will probably not reach the boiling zone and consequently have a retarded growth rate. We include this phenomenon in a length-dependent growth rate function given by Eq. 19, which is also used to describe attrition.

Secondary nucleation. In many papers evidence is found for the fact that primary nucleation will not occur in dense slurries at moderate growth conditions. Therefore, we assume nucleation to be predominantly secondary nucleation. Further, we assume that nucleation takes place only at the left boundary x_0 of the crystal size domain.

Secondary nucleation indicates that nuclei will originate only because of the presence of other crystals. These secondary nuclei are assumed to originate from two different breeding mechanisms (Daudey et al., 1990): mechanical and surface breeding. Mechanical breeding is a surface abrasion effect that can even occur in undersaturated solutions. Surface breeding is an attrition phenomenon that depends strongly on the supersaturation via the surface structure of the crystals that is a result of growth.

Results presented by Garside and Larson (1978) confirm the presence of two sources of nuclei. Experiments with potash alum crystals revealed that the majority of the nuclei were in the size range 1–10 μm, and could be produced in supersaturated as well as undersaturated solutions. Additionally, fragments in the range up to 50 μm were formed only under conditions of growth, and the number of these fragments was proportional to the supersaturation level. In the framework of Daudey et al. these observations are classified as mechanical and surface breeding, respectively. Detailed models for surface breeding can be found in van der Heyden (1992).

The empirical models for secondary nucleation in a suspension crystallizer presented in the literature are mostly power law models (Randolph and Larson, 1988; Garside, 1985; Mersmann et al., 1988; Van der Heyden, 1992). These models can describe both mechanical and surface breeding phenomena by relating the effective nucleation rate to the growth rate and the saturation condition of the mother liquor, on the one hand, and the presence of other particles, which are subject to particle-particle and particle-impeller interactions, on the other hand.

In this work also a power law model is used; however, we extended this model with an additional parameter p_4, which represents a lower bound of integration

$$B(t) = p_3 \left[\int_{p_4}^\infty n(x, t) x^{p_5} \, dx \right]^{p_1} \Delta C(t)^{p_2}, \tag{16}$$

with $p_1, \ldots, p_5$ empirical constants. The factor p_3 describes the combined effect of stirrer speed, pump rotation rate, slurry temperature, crystallizer geometry and so on with $p_u > 0$. This model excludes the contribution of small crystals to secondary nucleation, as these crystals are exposed to insignificant hydrodynamic and mechanical forces compared to large crystals. From simulation studies we found that CSD cycles can be described with this model, without the physical

meaningless values for the powers, which are needed to describe cycles with the standard power law model.

Crystal growth kinetics. The mechanism of crystal growth from solution requires that solute is transported to the crystal surface and incorporated into the crystal lattice. Two successive steps are required: a diffusion step, which is followed by a surface integration step. In some cases it is assumed that a growth rate distribution function exists for crystals of the same size. This phenomenon is called growth rate dispersion (GRD). The effect of GRD on the CSD will be most pronounced in the range of smaller particles ($x < 100$ μm). However, accurate on-line measurement of smaller particles in a crystallizer is difficult because of the lack of sufficiently accurate sensors. Therefore, in the first instance GRD is omitted also to prevent overparametrization of the model.

A standard power law model is used to describe the kinetic growth rate as a function of the supersaturation (Randolph and Larson, 1988):

$$G_k(t) = p_6 \Delta C(t)^{p_7}. \tag{17}$$

For an ideal MSMPR crystallizer the stationary CSD will be described by a straight line in the log population density plot (Randolph and Larson, 1988). In practice a CSD will decrease after a certain size (Pohlish and Mersmann, 1988; Jager, 1990). This phenomenon is called crystal growth retardation. The retardation of the crystal growth rate can be the result of attrition or length-dependent growth and spatial segregation of large particles, as already discussed. Attrition of crystals is an abrasion or surface erosion effect that describes the reduction in size of crystals due to collisions among crystals or crystals and the crystallizer hardware. The attrition rate is in principle related to the rate of nucleation. In Jager (1990), Pohlish and Mersmann (1988), and Mersmann et al. (1988) different models for the attrition of large crystals are presented. Here the attrition rate is modeled as a length-dependent growth function. To prevent overparameterization of the model, the same function is also used to describe the retardation of growth caused by spatial segregation of larger particles. Note that a direct coupling between secondary nucleation and attrition could therefore not be made in the model.

The effective growth rate is assumed to be the product of the kinetic growth rate and the length-dependent growth function:

$$G_e(x, t) = G_k(t) G_x(x). \tag{18}$$

The empirical model for this length-dependent growth function is chosen to be

$$G_x(x) = 1 - \frac{x^{p_8}(x_e^{p_8} + x_a^{p_8})}{x_e^{p_8}(x^{p_8} + x_a^{p_8})}, \tag{19}$$

which is an S-shaped curve, with x_a as the point of inflection and x_e as the maximum simulated crystal size, both parametrized by the unknown parameters p_9 and p_{10}, respectively. The sharpness of this curve is parametrized by p_8. An example of this function is given in Figure 3. The total set of kinetic parameters is denoted as $\theta_K = \{p_1, \ldots, p_{10}\}$.

Initial state

The initial state of the crystallizer considered here is the initial CSD and the initial saturation of the mother liquor (Eqs. 21 and 24). The initial CSD can originate from a distribution of seed crystals or results from heterogeneous primary nucleation in a crystal-free supersaturated liquid.

A Rosin-Rammler distribution is chosen for the initial CSD of the crystallizer. This distribution fitted best to the experimental data; however, simulation results indicate that other distributions like a log-normal or an inverse gamma distribution give comparable results. The Rosin-Rammler distribution contains three parameters: $\theta_S = \{p_{i1}, p_{i2}, p_{i3}\}$ related to the location, the spread, and the height of the initial CSD:

$$n_s(x) = p_{i1} p_{i2} p_{i3} (x^{p_{i2}-1}) \exp(-p_{i1} x^{p_{i3}}). \tag{20}$$

The initial supersaturation is assumed to be known.

Balance equations

The empirical relations are embedded in a set of balances to obtain a parametrized model for the crystallizer dynamics. A population balance is used to describe the dynamics of the CSD. A heat balance together with a set of mass balances for, respectively, the solution, the solvent, and the solids concentration in the slurry, describes the dynamics of the slurry properties. For the mass balances, a crystal mass, a salt mass, and a total mass balance are used. A detailed description of these balances is provided in the Appendix for the class of well-mixed, nonisothermal, nonconstant volume, batch as well as continuous, and evaporative as well as cooling-type crystallizers. These equations can easily be adapted to describe a cascade of crystallizers, or a crystallizer that is equipped with a clear liquor advance.

The reduction of the general model equations to a set of simplified equations is illustrated for the case of a continuous DTB-type crystallizer that was also used for the experimental work presented in this article.

For this crystallizer the following additional assumptions are made: the crystal volume is constant; the temperature is constant; the heat of crystallization P_{cryst}, the heat loss P_{loss}, and the heat from pumps and impellers P_{imp} are negligible compared to the heat consumed for solvent evaporation; no aggregation of crystals occurs; the feed flow Q_i has a constant temperature and is free of crystals; the stirrer speed is constant; the vapor flow Q_v contains no solute or crystalline material; and nucleation takes place at a negligible small size x_0, so $\Psi_1 = 0$ (Eq. A3).

Population balance. With these assumptions the population balance Eq. A1 is written as

$$\frac{\partial n(x, t)}{\partial t} + \frac{\partial G_e(x, t) n(x, t)}{\partial x} + \frac{Q_f(t)}{V} \gamma_f(t) h_f(x, t) n(x, t) + \frac{Q_{pf}(t)}{V} h_p(x, t) n(x, t) = 0, \tag{21}$$

with the boundary condition:

$$n(x = x_0, t) = B(t)/G_e(x_0, t) \tag{22}$$

and the parametrized initial condition: $n_s(x, t = t_0, \theta_S)$. Note that the factor γ_f is introduced here, because $Q_f(t)$ is used instead of the unclassified slurry flow Q_{ff} (Eq. 7).

Supersaturation balance. Several internal variables from the balances presented in the Appendix can be eliminated with algebraic substitutions. First a concentration balance is obtained by substitution of the crystal mass balance (Eq. A5) in the salt balance (Eq. A6). Substitution of

$$\Delta C(t) = C(t) - C_s \tag{23}$$

gives an expression for the supersaturation. Substitution of the crystal-mass balance (Eq. A5) in the total mass balance gives an expression for the input flow Q_i. An expression for the vapor flow is obtained by substitution of Eqs. A11 and A9 in the heat balance (Eq. A8). Substitution of the expressions for Q_i and Q_v in the supersaturation balance then results in the following balance for the supersaturation:

$$\begin{aligned}\frac{d\Delta C(t)}{dt} = \frac{1}{V\epsilon(t)}\Bigg[\Bigg[& -Q_p(t) - Q_f(t)[1-\epsilon_f(t)] \\ & + \frac{\Psi_2(t)}{\rho_c}\Bigg]\Delta C(t) + k_{c1}Q_{pf}(t) \\ & + k_{c2}Q_f(t)[1-\epsilon_f(t)] + k_{c3}Q_f(t) + k_{c4}P_{\text{tot}}(t) \\ & + k_{c5}\frac{\Psi_2(5)}{\rho_c}\Bigg],\end{aligned} \tag{24}$$

in which k_{c1}, k_{c2}, k_{c3}, and k_{c4} are constants calculated from physical properties of the crystallizer and the substance system. The variable $\Psi_2(t)$, which describes the consumption of dissolved crystal mass by growth, is given by Eq. A4. Note that for classified product removal Eq. 14 should be substituted for the product flow Q_p.

Sensor modeling

The population balance model is extended with a sensor model to compare the measured sensor output with simulated CSDs. Modeling of a sensor is illustrated for a forward-light-scattering-based sensor, which is commonly used in CSD sensing. This sensor is also used in the experimental work discussed below.

A model based on the Fraunhofer diffraction theory is determined. A scatter matrix is developed for rectangularly shaped crystals with an average aspect ratio α, assuming that only their rectangular shapes are projected on the detector plane. Based on formulas presented by Hecht (1987), a sensor model is derived that describes the light intensity observed on a certain detector location as a function of the crystal size and the aspect ratio. Integrating this model over a set of crystal size intervals and detector rings results in the following sensor model:

$$L = G(\alpha)n, \tag{25}$$

with G the sensor model matrix, L the light intensity vector measured on the detector rings, and n a discrete population density.

Inversion (deconvolution) of the model, given by Eq. 25, can be used to calculate the size distribution from an averaged intensity vector L and the corresponding noise covariance matrix (Boxman et al., 1991). The resulting CSD describes a volume distribution based on a grid with logarithmic equidistant size classes and is denoted as $n_v(x, t)$.

From these, characterizing quantities are calculated. Robust parameters are derived from the quartiles of the size distribution, defined by

$$\int_{x=0}^{X_k} n_v(x)\,dx \triangleq \frac{k}{100}, \quad \text{with} \quad k = 25, 50, 75, \textit{and } 100. \tag{26}$$

The second quartile, the median (X_{50}), is taken as a measure for the location of the CSD, and the logarithmic interquartile range

$$qr \triangleq \ln \frac{X_{75}}{X_{25}}, \tag{27}$$

is taken as a measure for the spread.

In this article these robust parameters derived from the deconvolution step are solely used for presentation purposes. The estimation of empirical parameter values, which is discussed below, is based directly on the raw sensor data, to eliminate numerical uncertainties that can evolve from the deconvolution algorithm (Boxman et al., 1991) and to obtain a statistically better conditioned error criterion.

Parameter Estimation

The process model obtained in the previous section is a parametrized model for an evaporative isothermal constant volume crystallizer, and includes models for the process actuators given by the separator model equations: Eqs. 8 and 13, as well as the CSD dynamics given by Eqs. 16–19, 21, 22 and 24, and the CSD sensor, which is described by Eq. 25. The total set of unknown model parameters is denoted as $\theta = \{\theta_K, \theta_S, \theta_C\}$. The classification parameters θ_C are estimated in the first step. In the next step the optimal fines classification functions are incorporated in the population balance model and the remaining set of parameters ($\{\theta_S, \theta_K\}$) are estimated.

For estimation of parameters based on the raw light intensity data the following general criterion is used:

$$J(\theta) = \sum_{j=1}^{k}\sum_{i=1}^{m} \frac{[L_i(j) - \hat{L}(\theta)_i(j)]^2}{\sigma_i(j)}, \tag{28}$$

with m the number of detector rings and k the total number of samples. The term $\hat{L}(\theta)_i(j)$ is the light intensity at ring i and time instant j predicted by the model as a function of the parameter vector θ. The term $L_i(j)$ is an average intensity vector calculated from a large (> 100) number of detector readings (sweeps). The variance of the fluctuations around the average, σ_i, $i = 1, \ldots, 31$, is used as a weighting factor for the quadratic errors. The general quadratic criterion uses

the full covariance matrix of the sweeps to weight the errors; however, only the diagonal elements of this matrix were available from the data acquisition system that was used. Inspection of the weighted errors revealed that all errors contribute to the total error with the same order of magnitude.

Both measured and predicted light intensity vectors used in the criterion are scaled in such a way that the total sum of the respective vector elements equals unity. This scaling is essential as the total intensity is corrupted by an unknown and randomly varying dilution factor, caused by the slurry diluter, which is introduced below.

Parameter estimation is applied to find the minimizing argument $\hat{\theta}$ for this criterion. The nonlinear gradient-based optimization module E04UCF provided in the NAG library can be used to solve this problem.

Equation 21 is approximated by applying the so-called method of lines. The derivative in the size domain is approximated by a simple second-order method of lines scheme (de Wolf, 1990), which is second-order accurate. The integrals given by Eqs. 6 and A3 are approximated by a second-order accurate integration scheme. Time integration of the lumped population balance is performed with the forward Euler method with truncation error correction, introduced by Ceschino and Kuntzman (1963). Use is made of software modules provided by Schiesser (1987).

A rough estimate of the confidence of the estimated parameters is obtained by calculating the standard deviation of the parameters obtained for the different data sets. More advanced methods like Monte Carlo studies or methods based on residual evaluation (Bard, 1974; Rawlings et al., 1993) to assess parameter confidence intervals are not applied here because the model residual is not a Gaussian white process and because Monte Carlo studies ask for an unacceptable computation time.

Experimental Setup

A series of experiments is performed with a continuous draft-tube baffled crystallizer equipped with an annular zone around the crystallizer vessel in which classified removal of fine particles is established. Unclassified product is removed. A schematic drawing of this crystallizer is given in Figure 4. PI control loops are present in the process to keep the slurry temperature, the crystallizer volume, the fines and product removal flow, the temperature of dissolved fines, and the total heat input at a prescribed set-point value. With the forward-light-scatter sensor the dynamic CSD response on the unseeded startup of the pilot crystallizer is measured for different process input parameter values. The initial CSD of the unseeded crystallizer results from primary heterogeneous nucleation occurring in the supersaturated mother liquor. The information content of process startup data is considered to be large, and plant startup data are often readily available in industrial practice, since processes have to be shut down frequently for cleaning or maintenance purposes.

Unclassified product is removed during the experiments, that is, $h_p = 1$ and $Q_p = Q_{pf}$. The startup CSD response is measured over a period of approximately 40 hours, as a function of three different values of the retention time of product, three fines removal rates, and three values for the total heat input. The crystallizer is fed with slightly undersaturated

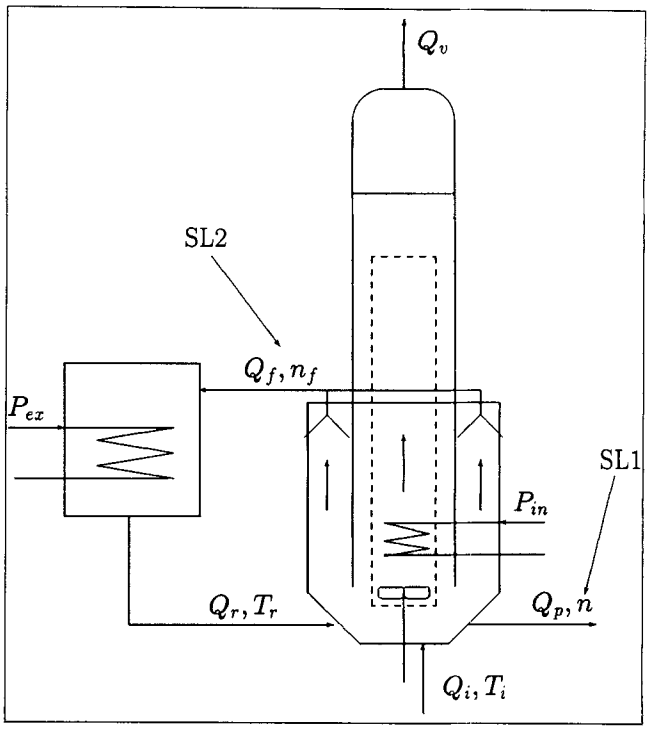

Figure 4. Evaporative draft tube baffled pilot crystallizer, equipped with a fines removal system.

free liquid crystal. The crystal slurry is transported with low speed Mohno pumps to minimize abrasion. A condenser is used to extract vapor. Heat is supplied by an internal heat exchanger that is positioned in the draft tube, and an external heat exchanger that is used to dissolve fines. A rubber-coated marine-type impeller is used as a pumping device to keep the crystals circulating as a suspension. The removed fines are dissolved by increasing the temperature of the fines flow by 10°C before recycling. The cross-sectional area of the fines classifier is 0.7461 m^2. The feed flow (Q_i) to the crystallizer is just saturated at 50°C. The feed temperature (T_i) is slightly raised, and the flow is filtered before entering the vessel to ensure a crystal-free feed that is slightly undersaturated.

For the first experiment referred to as EXP1, the controlled process conditions, which are kept unaltered during the experiments, are tabulated in Table 1. This first experiment is succeeded by a series of experiments where one process input variable at the time is varied compared to EXP1. The specific conditions are tabulated in Table 1.

During the experiments CSD measurements are taken at two different locations: the unclassified product flow (Q_p), which is isokinetically withdrawn from the crystallizer, and the fines flow (see also Figure 4, SL1 and SL2, respectively). The scattered light is recorded at 31 detector elements by two Malvern 2600 Particle Sizers with two different collimating lenses. A 300-mm lens is mounted to observe the fine crystals at SL2 and a 1,000-mm lens is used to observe the crystals at SL1. In the deconvolution step a relative volume distribution on 20 size classes is calculated based on a loga-

Table 1. Set-Point Values for Local PI-Controllers

Experiment Number	Variable	Value
EXP1	Fines flow	1.0 L/s
	Total heat input	120 kW
	Product flow	0.22 L/s
	Stirrer speed	350 rpm
	Temperature fines	60°C
	Temperature vessel	50°C
	Volume	970 L
EXP2	Fines flow	2.2 L/s
EXP3	Fines flow	3.4 L/s
EXP4	Product flow	0.15 L/s
EXP5	Product flow	0.39 L/s
EXP6	Total heat input	90 kW
EXP7	Total heat input	150 kW

rithmic grid with 23 percent resolution, that is, the width of successive logarithmic classes increases by a factor 1.23.

The sampling frequency is kept at a rate of one sample per 2 minutes. Because the crystal volume in the slurry is too high for direct measurement, a dilution unit is designed that dilutes slurry samples on-line with saturated mother liquid. This unit also enables automatic background measurements that are needed to correct for transients due to nonconstant laser intensity or fouling of the optical cell. Outliers caused by blockage of the measurement system are removed by an automatic peak-shave procedure.

Results and Discussion

Experimental data

Figure 5 and 6 show the dynamic response of X_{50} and qr (defined by Eqs. 26 and 27) on the initial CSD of an unseeded crystallizer for three different fines removal flows: 1.0, 2.2, and 3.4 L/s (EXP1, EXP2, and EXP3), respectively. Also

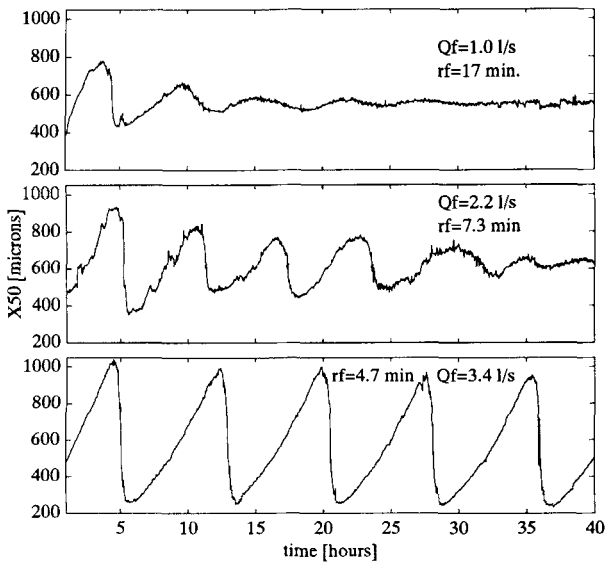

Figure 5. Experimental time response of the median crystal size at startup with a fines flow of 1.0, 2.2, and 3.4 L/s (EXP1, EXP2, and EXP3), respectively.

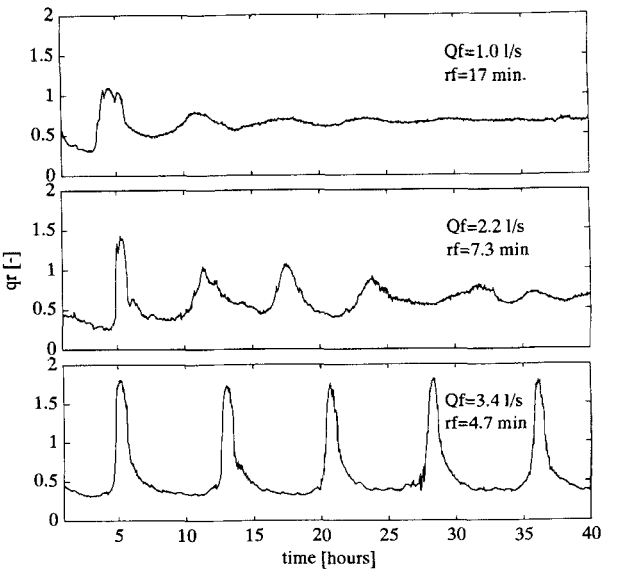

Figure 6. Experimental time response of the quartile ratio at startup with a fines flow of 1.0, 2.2, and 3.4 L/s (EXP1, EXP2, and EXP3), respectively.

in these plots the so-called mother liquor retention time, given by $r_f = V/Q_f$, is printed. These figures reveal that fines removal promotes cycling and even induces a limit cycle in the CSD. The quartile ratio peaks at the time when the median crystal size collapses. This indicates the existence of a temporal bimodal-shaped distribution in which both large and newly born small crystals are present.

Figure 7 shows the dynamic response of X_{50} for three different product removal flows: 0.39, 0.22 and 0.15 L/s (EXP5, EXP1, and EXP4), respectively. It can be seen that the time period of oscillations is approximately proportional to the retention time of product r_p. This can be explained by the fact that increasing the product flow will mainly decrease the total crystal surface area available for growth and therefore accelerate the kinetic growth rate of the crystals, which subsequently increases the speed of response. Note that industrial crystallizers normally operate at larger retention times, which explains why they exhibit larger oscillation time/periods than the pilot crystallizer used here.

Figure 8 shows the influence of three different values for the total heat input: 90, 120, and 150 kW (EXP6, EXP1, and EXP7), respectively. The measured trend of EXP6 is disturbed approximately 18 hours after startup by a rinse water flow. These plots show that the influence of a varying heat input on the startup CSD dynamics is insignificant. Variations in the heat input will, however, proportionally change the crystal mass production rate at stationary conditions.

During EXP1, EXP2, and EXP3, fines distributions were measured at sample location SL2. The relative volume distribution of fines corresponding to a specific fines flow varied only slightly in time. Therefore average fines distributions were calculated for the three different fines flows. Figure 9 demonstrates how the cut-size of the fines classifier shifts to larger values for larger fines flows. In Figures 10 and 11 the raw light intensity distributions, as observed at sample location SL1 during EXP1 and EXP3, are depicted, respectively.

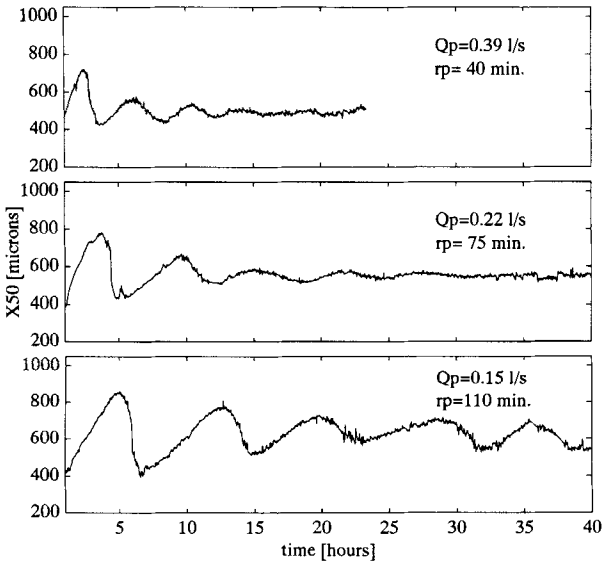

Figure 7. Experimental time response of the median crystal size at startup with a product removal flow of 0.39, 0.215 and 0.15 L/s (EXP5, EXP1, and EXP4), respectively.

For the experiments EXP1, . . . , EXP7 these raw intensity data, recorded directly from the Malvern sensor, are used to estimate the model parameters θ.

Estimation of the fines classification function

The fines classification function was estimated from data obtained at both sample locations SL1 and SL2. As delays and dynamics are assumed to be negligible, the estimation of this function is a static nonlinear function estimation problem, where the nonlinear function h has to be estimated from raw light intensity data L. We solved this problem by formulating it as a prediction problem. First we estimated the product size distribution by inverting the model Eq. 25, after which the light intensity observed on the detector located at SL2 is predicted by the following equation:

$$\hat{L}_f = G_f \gamma_f \text{diag}\{\hat{h}_f(\theta_c)\}\hat{n}_p \tag{29}$$

where $\hat{n}_p$ represents the estimated product size distribution obtained by inverting the model Eq. 25, G_f is the sensor model that is calculated for the fine particles, and $\text{diag}\{\hat{h}_f(\theta_C)\}$ is the discretized diagonal removal matrix parametrized with the fines separation parameters $\theta_c = \{p_{f1}, p_{f2}\}$. Because the different void fractions did not change significantly, the flow split factor was approximated by $\gamma_f = 1.12$. The average shape factor α was estimated to be 1.4. Now the quadratic criterion Eq. 28, together with the optimization routine, is used to

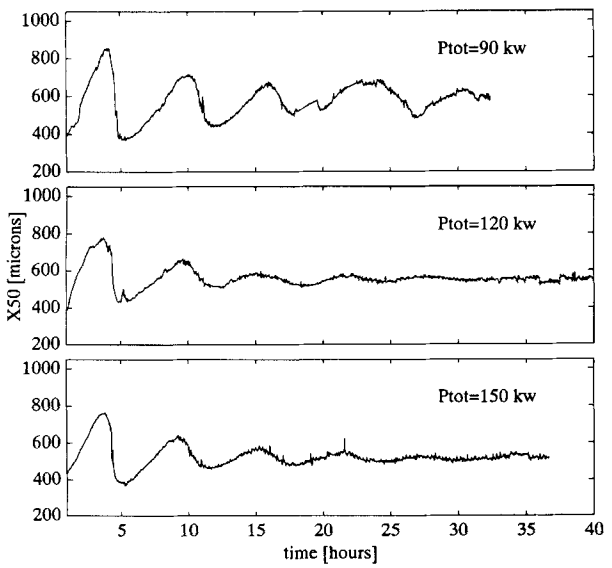

Figure 8. Experimental time response of the median crystal size at startup with a total heat input of 90, 120, and 150 kW (EXP6, EXP1, and EXP7), respectively.

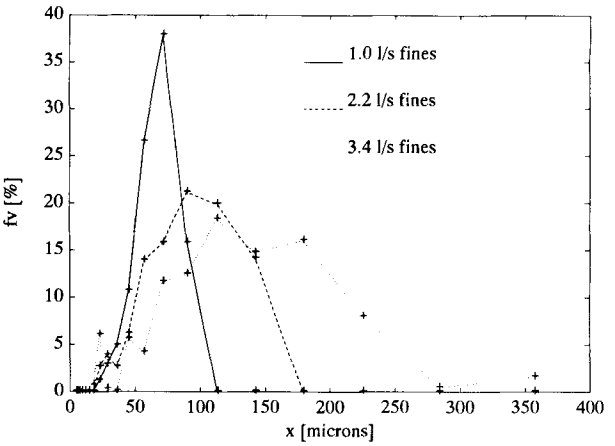

Figure 9. Experimental relative volume-based CSD of fines for fines removal flows of 1.0, 2.2, and 3.4 L/s, (EXP1, EXP2, and EXP3), respectively.

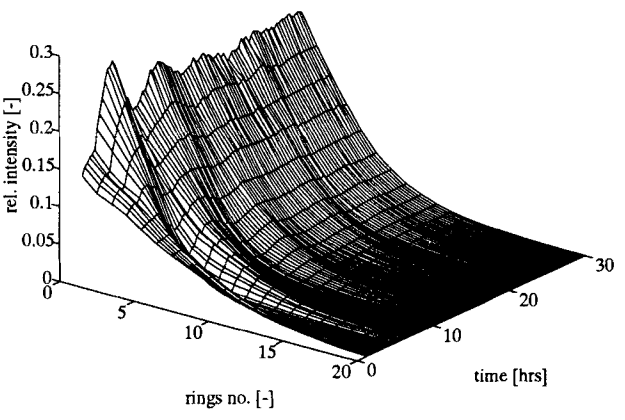

Figure 10. Experimental time response over 30 hours of the scaled light intensity on the first 20 detector rings for a fines removal flow of 1.0 L/s (EXP1).

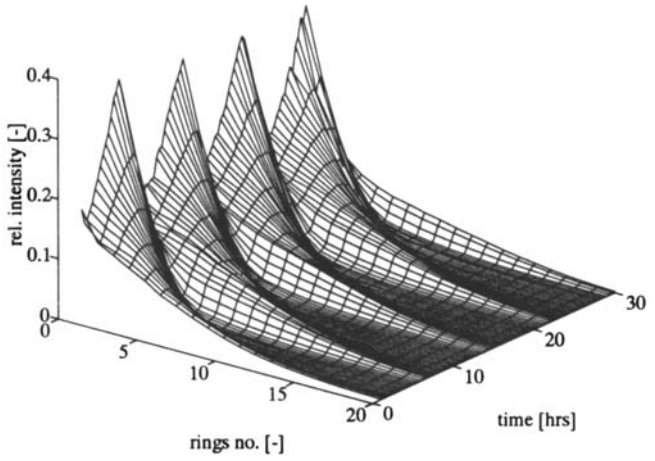

Figure 11. Experimental time response over 30 hours of the scaled light intensity on the first 20 detector rings for a fines removal flow of 3.4 L/s (EXP3).

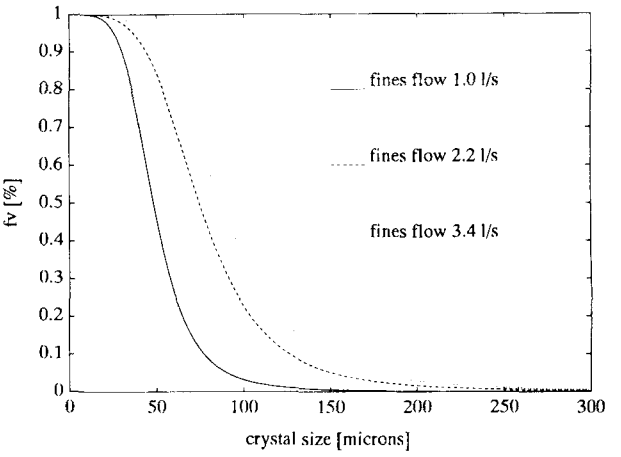

Figure 12. Estimated fines classification curves.

minimize the difference between the predicted and measured values for L_f as a function of the parameters θ_c.

This scheme is used to estimate the parameter values p_{f1} and p_{f2} of the fines classification function given by Eqs. 8 and 9, based on data sets obtained during three different runs: EXP1, EXP2, and EXP3. The estimated parameter values are listed in Table 2, together with their average value and the corresponding standard deviation. In the last column of Table 2 the estimated cutsizes are given. They were calculated from Eq. 9. The corresponding estimated removal probability curves are plotted in Figure 12. The estimated efficiency curves show the expected shift of the removal probability curve to the range of larger crystal sizes for larger fines removal flows.

Estimation of kinetic parameters and initial state

Prior to the estimation of parameters a parameter sensitivity analysis is made by perturbing parameters from the set θ_K, and inspection of the resulting perturbation of the criterion (Eq. 28). The parameters p_2, p_6, p_7, and p_{10} were denoted as insensitive parameters and were given the following fixed values: $p_2 = 0.0$, $p_6 = 10^{-8}$, $p_7 = 1.0$, and $p_{10} = 1{,}850 \times 10^{-6}$. An important result of this preliminary study is that the influence of supersaturation on the secondary nucleation rate (Eq. 16) can be neglected. The remaining set of parameters to be estimated is given by $\{p_1, p_3, p_4, p_5, p_8, p_9, p_{i1}, p_{i2}, p_{i3}\}$.

Table 2. Estimated Fines Classification Parameters

Exp. No.	$\hat{p}_{f2}$	$\hat{p}_{f1}[\cdot 10^{-5}]$	x_c [μm]
EXP1	4.68	0.232	48.2
EXP2	4.17	0.252	74.5
EXP3	4.21	0.223	87.1
Avg.	4.35	0.236	
Std. Dev.	0.23	0.012	

The nucleation model (Eq. 16) is scaled by the stationary solution of the population balance to improve the parameter sensitivity, which strongly influences the numerical condition of the estimation problem (Bard, 1974). After scaling of Eq. 16 the parameter p_3 equals the steady-state value of the nucleation rate and the remaining parameters in this equation $\{p_1, p_2, p_4, p_5\}$ solely affect the nucleation rate when the process is not stationary.

At first the parameter estimation results revealed a significant bias between the model and measured values of the large detector rings numbered $i = 18, \ldots, 31$, as depicted in the upper plot of Figure 13. From light scattering theory it is known that the smaller particles scatter relatively strongly on the larger detector rings. We therefore adopt the idea of adding a second distribution, representing slowly growing fines, to the distribution predicted by the model. This added distribution should account for a model deficit in the region of small particles. A simulation study demonstrated that the model mismatch can be compensated with a constant expo-

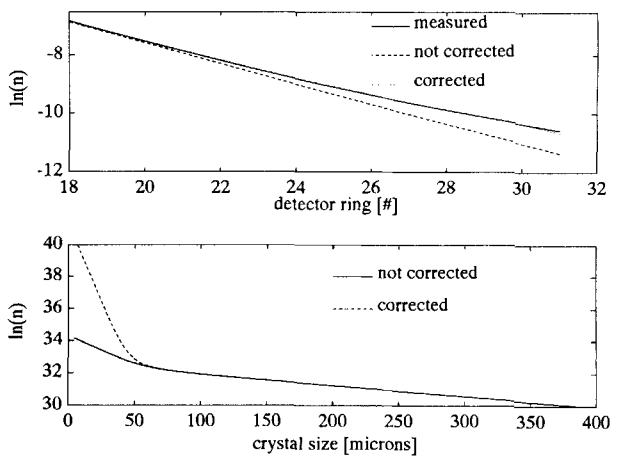

Figure 13. Measured, not corrected, and corrected light intensity distributions (upper) and the corresponding uncorrected and corrected simulated ln(n)-x plots (lower).

nential distribution given by

$$n_2(x) = k \exp\left(-\frac{Q_f + Q_p}{VG_2}x\right), \tag{30}$$

with G_2 the constant growth rate of the population of slowly growing fines ($G_2 < G_k$), and $Q_f + Q_p$ the removal rate of small particles. The linear factor k is calculated from a simple least squares fit on the error. In Figure 13 it can be seen that the error is indeed strongly reduced and that the added distribution has strongly magnified the estimated CSD in the region of small crystals. The average growth rate of the added crystal population was estimated to be 0.45×10^{-8} m/s, which is roughly ten times slower than the growth rate G_k of the modeled crystal population. This result points at a large population of small crystals with a very slow growth rate. The validity of this conclusion can, however, be questioned for two reasons: the recorded light intensity distributions are corrected for the background signals that are measured. These corrections do not accurately account for the presence of particles in the optical cell. Secondly, results presented by Brown et al. (1991) indicate that anomalous diffraction can occur. Anomalous diffraction occurs when the ratio of the solid-to-medium (liquid) refractive indices are close to unity. In this case light will also travel through the particle. Mie theory can be used to account for this effect. The results presented by Brown indicate that the Mie model, for ammonium sulphate crystals with a refractive index of 1.08, will predict more energy on the larger rings than the Fraunhofer model used here, and therefore can (partially) account for the deviation we observed here. The Mie model is not applied since no software was available for its evaluation.

Therefore, if more information is wanted on growth rate dispersion, more accurate sensor models and probably more sensitive CSD sensors, which focus specifically on the region of small crystals, are needed. In the current approach our model describes effective phenomena such as the effective secondary nucleation rate, and a possible model deficit in the region of small crystals is only corrected to prevent the estimated effective parameters from getting biased.

In Table 3 the three parameter values for the initial distributions estimated for the different data sets, together with their average value and the corresponding standard deviation are given. In Table 4 the estimated values for the nucleation and growth rate parameters are listed together with their average and standard deviation. Corresponding model fits are depicted in Figures 14 and 15, for three different detector rings $\{j = 5, 10, 20\}$, for EXP1 representing the best fit, and EXP3 representing the worst fit. All other fits are comparable to the result obtained for EXP1. The larger model mismatch and biased parameter values corresponding to the data from EXP3 are probably caused by aggregation or primary nucleation during the strong nucleation burst that occurred when the median reaches a peak value (Figure 5). These phenomena are not included in the model.

Table 3. Parameters Related to Initial Condition

Exp. No.	p_{i1} [$\times 10^8$]	p_{i2}	p_{i3} [$\times 10^{10}$]
EXP1	5.83	2.41	0.46
EXP2	9.26	2.60	1.53
EXP3	9.55	2.87	0.39
EXP4	4.17	2.38	0.46
EXP5	2.42	2.35	0.61
EXP6	4.03	2.37	0.49
EXP7	6.92	2.39	1.55
Avg.	6.03	2.48	0.78
Std. Dev.	2.51	0.17	0.48

Table 4. Parameters Related to Growth and Nucleation Kinetics

Exp. No.	p_1	p_3 [$\cdot 10^8$]	p_4 [$\cdot 10^{-6}$]	p_5	p_9 [$\cdot 10^{-6}$]	p_8
EXP1	0.76	0.10	674	2.76	1,191	5.97
EXP2	1.15	1.23	519	2.06	1,060	6.92
EXP3	2.00	0.61	1,002	2.01	983	6.00
EXP4	0.85	0.08	765	3.18	868	11.55
EXP5	0.55	0.09	666	1.34	1,210	10.66
EXP6	1.49	0.07	610	2.07	924	8.10
EXP7	0.71	0.20	621	1.64	805	12.13
Avg.	1.07	0.34	694	2.15	1,006	8.76
Std. Dev.	0.48	0.40	144	0.58	144	2.45

It can be concluded from Figure 14 that the model gives a reasonable fit of the CSD dynamics. The nucleation parameters provide the best fit if the nucleation rate is taken to be proportional to the total surface area of particles with sizes larger than approximately 600 μm. Such a dependence on the total surface area instead of the mass of the CSD points to surface breeding. The low sensitivity of parameter p_2 (which was kept constant), however, shows that the influence of supersaturation on the observed CSD dynamics is low, which is not expected in the case of surface breeding. The values found for p_1 and p_5 agree with values provided in the literature (Garside, 1985). Some parameter values, especially p_3, are uncertain. This uncertainty can be caused by differences in experimental conditions, like an alternating un-

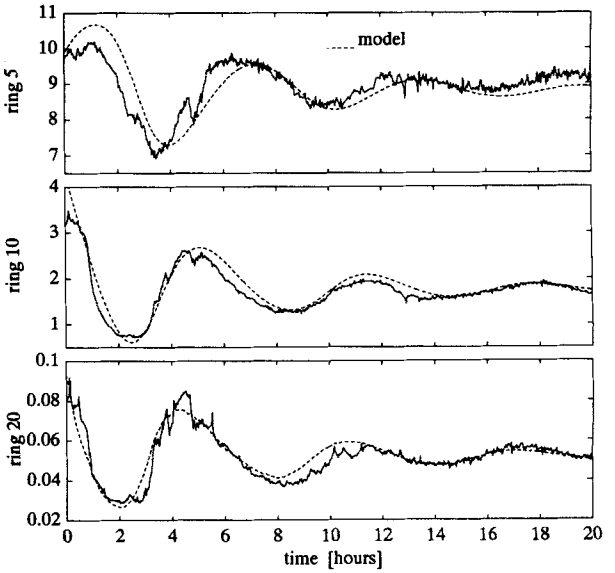

Figure 14. Model (dashed) and process response for detector rings [5, 10, 20] corresponding to EXP1.

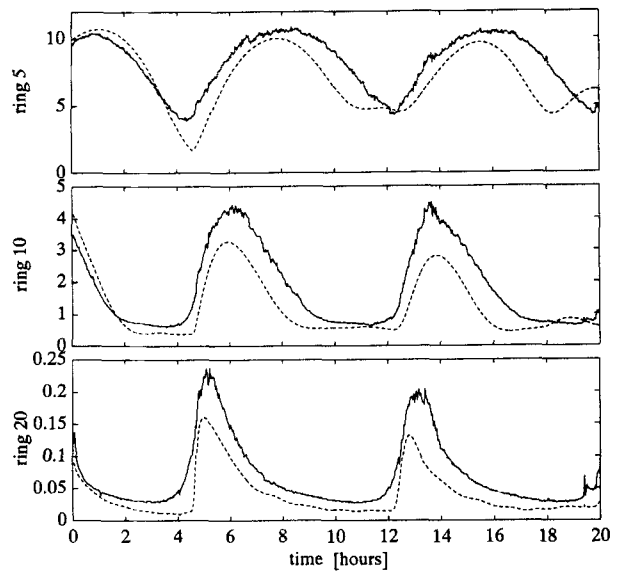

Figure 15. Model (dashed) and process response for detector rings [5, 10, 20] corresponding to EXP7.

known impurity concentration, or the limited sensitivity of the sensor for the phenomena to be estimated. Better results are expected with a sensor that is more sensitive to large and small particles. Additionally, robustness analysis of the controller that is designed on the basis of this uncertain model will be important (Eek et al., 1995).

Figure 16 gives the $\ln(n)$-x plots corresponding to the model fit to EXP1 at three different time points T = 3, 6, 40 hours. This plot illustrates how badly dampened or oscillatory CSD dynamics can be explained by a simple secondary nucleation mechanism in which only large particles play a significant role: particle waves come up in the region of small crystals and grow into the region of large crystals $x > 600$ μm in a time period of approximately 3 hours, then a new wave of small particles or new nuclei is initiated from attrition fragments

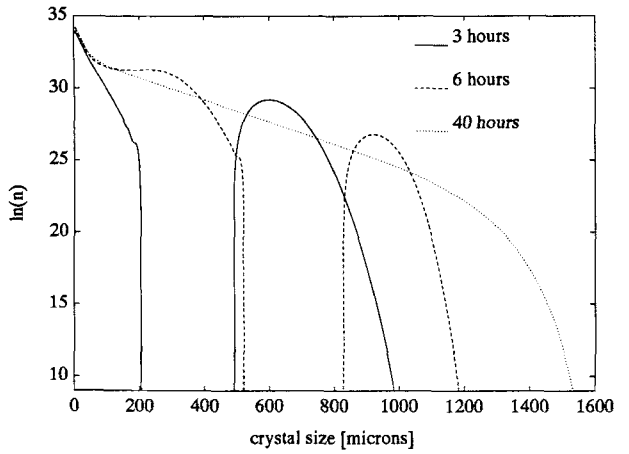

Figure 16. Simulated $\ln(n)$-x plot corresponding to EXP1 at three different times.

bred on the surface of larger crystals. At the moment these new nuclei are formed, the total surface area of the crystals is relatively low and the supersaturation will rise because of a lack of consumption of ammonium sulphate molecules. This will increase the growth rate providing a large portion of the newly formed fines with a chance to survive the fines trap. In the initial stage of their outgrowth the total surface area will increase and the growth rate will decrease again, which strongly reduces the chance that small particles will survive the fines trap. This mechanism explains the destabilizing effects of fines removal.

The described mechanism is more complicated when the process includes a product classifier that enables the selective removal of large product particles from the crystallizer volume. This topic is being studied at this moment. Furthermore the presented models are only validated for one specific geometry and scale. Therefore, a major topic for future research should be the inclusion of hydrodynamic models (Jager, 1990).

Conclusions

The model that is presented describes the dynamics of a pilot scale suspension crystallizer in a reasonable way.

- Extending a crystallizer model with a sensor model is advantageous since it eliminates numerical errors introduced by sensor model inversion and achieves consistent treatment of particle size and shape throughout the model.
- CSD dynamics can be influenced by fines and product removal. Varying the heat input has a less significant effect on CSD dynamics and mainly effects the mass production rate. Fines removal promotes CSD cycling. Varying the mean slurry residence time gives a proportional change in the time period of oscillations.
- Nonlinear parameter estimation is a flexible method for obtaining estimates for unknown model parameters. Using a quadratic criterion in which errors are calculated directly from raw sensor data and weighted with the estimated variance is advantageous since it effectively penalizes less reliable data subject to large random variations.
- A fairly simple secondary nucleation model, containing physically interpretable parameter values, describes oscillatory or badly dampened CSD dynamics. The estimated secondary nucleation model shows that the effective secondary nucleation rate is proportional to the total surface area of particles, with a size larger than approximately 600 μm.
- The results further indicate that the growth of larger particles is hampered, which is explained by both attrition and spatial segregation of larger particles, and is described sufficiently accurate by a simple S-shaped length-dependent growth curve.
- Some evidence is found for the existence of a large population of slowly growing fines, with a growth rate that is approximately ten times lower than the normal growing crystals.

The results of our study have shown that models for CSD dynamics can be obtained from a nonlinear parameter estimation procedure based on a parameterized physical model including submodels for the CSD sensor, the CSD actuators, and the initial state. These models will form a good basis for the design and analysis of controllers for CSD dynamics,

which will finally enhance the performance of industrial crystallizers.

Acknowledgment

The authors would like to express their gratitude to the Dutch Foundation of Technology (STW), AKZO, ICI, DOW Chemicals, DSM, E.I. Dupont de Nemours, and Eastman Chemical Company for their financial support of the UNIAK research program.

Notation

A = cross-sectional area annular zone, m^2
B = secondary nucleation rate, $\#/m \cdot m^3$
c_p = specific heat, kJ/kg°C
C = concentration, kg/m^3
g = CSD sensor model
g = constant of gravity, m/s^2
G = CSD sensor model matrix
G_k = kinetic crystal growth rate, m/s
G_x = length-dependent crystal growth rate, m/s
G_e = effective crystal growth rate, m/s
h = removal probability function
H_v = specific enthalpy, kJ/(kg)
J = criterion value
k_c = constant related to class I crystal growth
k_v = volume-based crystal shape factor
L = light intensity distribution, J/m^2
m_j = jth moment of crystal size distribution, $\#m^j/m^3$
n = population density, $\#/m \cdot m^3$
N = cumulative number function, $\#/m^3$
p = empirical parameter
P = power input, kW
Q = flow rate, m^3/s
qr = quartile ratio
r = retention time of slurry, s
SL_i = sample location i
t = time, s
T = temperature, °C
V = volume of crystallizer vessel, m^3
x = crystal size, m
x_c = cutsize, m
X_k = k = {25, 50, 75} quartiles of distribution, m

Greek letters

α = aspect ratio of crystals
Δ = difference operator
μ = absolute viscosity, $kg/m \cdot s$
γ = flow split factor
ρ = density, kg/m^3
σ = standard deviation
θ = empirical parameter vector
ϵ = void fraction
ξ = constant factor related to specific heat, kJ/kg°C
Ψ_1 = contribution of birth-to-mass balances, $kg/m^3 \cdot s$
Ψ_2 = contribution of growth-to-mass balances, $kg/m^3 \cdot s$

Subscripts

0 = left boundary of spatial domain
$\hat{}$ = corresponding to estimated value
c = solid phase (crystals)
ex = external
f = related to fines removal
ff = feed of fines removal system
HC = heat exchanger
i = input flow; initial condition; ring index
j = time index
in = internal
l = liquid phase; related to particle length
p = related to product removal
pf = feed of product removal system
pr = return product removal system
r = return or recycle of fines and product
v = vapor; crystal volume based
w = related to particle width
$*$ = any flow

Literature Cited

Bard, Y., *Non-linear Parameter Estimation*, Academic Press, New York (1974).

Boxman, A., H. G. Merkus, P. J. T. Verheijen, and B. Scarlett, "Deconvolution of Light-Scattering Patterns by Observing Intensity Fluctuations," *Appl. Opt.*, **30**, 4818 (1991).

Brown, J. D., K. Alexander, and J. Cao, "Anomalous Diffraction Effect in the Sizing of Solid Particles in Liquids," *Part. Part. Syst. Charact.*, **8**, 175 (1991).

Ceschino, F., and J. Kuntzman, *Numerical Solution of Initial Value Problems*, Chap. 1, Prentice-Hall, Englewood Cliffs, NJ (1963).

Daudey, P., G. M. van Rosmalen, and E. J. de Jong, *J. Cryst. Growth*, **99**, 1076 (1990).

Eek, R. A., H. A. A. Pouw, and O. H. Bosgra, "Design and Experimental Evaluation of Stabilizing Feedback Controllers for Continuous Crystallizers," *Powder Technol.*, **82**, 21 (1995).

Garside, J., and M. A. Larson, "Direct Observation of Secondary Nuclei Production," *J. Cryst. Growth*, **43**, 694 (1978).

Garside, J., "Industrial Crystallization from Solution," Rev. Art. 15, *Chem. Eng. Sci.*, **40**(1), 3 (1985).

Jager, J., "Control of Industrial Crystallizers," PhD Thesis, Delft Univ. of Technology, Delft, The Netherlands (1990).

Hecht, E., *Optics*, 2nd ed., Addison-Wesley, Reading, MA (1987).

Leer, B. G. M., A. de Koning, and E. J. de Jong, "Stability and Dynamic Behaviour of Crystallizers," *Indust. Crystallization*, Plenum, New York, p. 391 (1976).

Hallas, N. J., and M. L. Hannan, "Measurement and Computation of Hydrodynamics for a Draft Tube Baffled Crystallizer," in *Proc. Symp. Industrial Crystallization*, A. Mersmann, ed., 107 (1990).

Van der Heyden, A. E. D. M., "Secondary Nucleation and Crystallization Kinetics," PhD Thesis, Nijmegen Univ., The Netherlands (1992).

Koskinen, T. J., and H. V. Norden, "Mathematical Model for the Classifier of a DTB Crystallizer," Part I, *kemia-kemi*, **4**, 205 (1979); Part II, *kemia-kemi*, **6**, 405 (1981).

Mersmann, A., R. Sangl, M. Kind, and J. Pohlisch, "Attrition and Secondary Nucleation in Crystallizers," *Chem. Eng. Technol.*, **11**, 80 (1988).

Pohlisch, J., and A. Mersmann, "The Influence of Stress and Attrition on Crystal Size Distribution," *Chem. Eng. Technol.*, **11**, 40 (1988).

Randolph, A. D., and M. A. Larson, *Theory of Particulate Processes*, Academic Press, London (1988).

Rawlings, J. B., S. M. Miller, and W. R. Witkowski, "Model Identification and Control of Solution Crystallization Processes: A Review," *Ind. Eng. Chem. Res.*, **32**, 1275 (1993).

Schiesser, W. E., *The Numerical Method of Lines; Integration of Partial Differential Equations*, Academic Press, San Diego (1987).

Svarovsky, L., *Solid-Liquid Separation*, Butterworth, London (1990).

Tavare, N. S., and J. Garside, "Simultaneous Estimation of Crystal Nucleation and Growth Kinetics from Batch Experiments," *Chem. Eng. Res. Dev.*, **64**, 109 (1986).

De Wolf, S., "Modeling, System Identification and Control of an Evaporative Continuous Crystallizer," PhD Thesis, Delft Univ. of Technology, The Netherlands (1990).

Appendix

Population, mass, and heat balances

All physical slurry parameters used are defined per cubic meter of slurry. More details on the derivation of mass and heat balances can be found in de Wolf (1990).

Population balance. The population balance describes the CSD dynamics in the crystallizer (Randolph and Larson, 1988):

$$\frac{\partial V(t)n(x,t)}{\partial t} + V(t)\frac{\partial G_e(x,t)n(x,t)}{\partial x} + Q_f(t)\gamma_f(t)h_f(x,t)n(x,t) + Q_{pf}(t)h_p(x,t)n(x,t) - Q_i(t)n_i(x,t) = 0, \quad \text{(A1)}$$

with the boundary condition:

$$n(x = x_0, t) = \frac{B(t)}{G_e(x_o, t)} \quad \text{(A2)}$$

and the parametrized initial condition, $n_s(x, t = t_0, \theta_S)$.

Crystal mass balance. Two additional equations for $\Psi_1(t)$ and $\Psi_2(t)$ are introduced, respectively, to include the effects of crystal growth and crystal birth in the mass balances:

$$\Psi_1(t) = V(t)\rho_c(t)k_v B(t)x_0^3, \quad \text{(A3)}$$

$$\Psi_2(t) = 3\rho_c k_v V(t)\int_0^\infty G_x(x)x^2 n(x,t)\,dx. \quad \text{(A4)}$$

The crystal mass in the crystallizer is described by the following equation:

$$\frac{d}{dt}[V(t)[1-\epsilon(t)]\rho_c(t)] = + Q_i(t)[1-\epsilon_i(t)]\rho_c(t) - Q_f(t)[1-\epsilon_f(t)]\rho_c(t) - Q_p(t)[1-\epsilon_p(t)]\rho_c(t) + \Psi_1(t) + \Psi_2(t). \quad \text{(A5)}$$

The void fractions ϵ are calculated according to Eq. 6, and ρ_c is the density of the crystals. The crystal mass balance can be derived directly from the population balance, Eq. 21; consequently, it does not add new information to the model.

Saltmass balance. The dynamic equation describing the mass of salt (dissolved crystal material and crystals) present in the crystallizer is given by

$$\frac{d}{dt}[V(t)[\epsilon(t)C(t)+[1-\epsilon(t)]\rho_c(t)]] = + Q_i(t)[\epsilon_i(t)C_i(t)+[1-\epsilon_i(t)]\rho_c(t)] - Q_f(t)[\epsilon_f(t)C(t)+[1-\epsilon_f(t)]\rho_c(t)] - Q_p(t)[\epsilon_p(t)C(t)+[1-\epsilon_p(t)]\rho_c(t)] + Q_r(t)C_r(t). \quad \text{(A6)}$$

Total mass balance. The balance for the total mass (clear liquid mass and crystal mass) is given by the following equation:

$$\frac{d}{dt}[V(t)[\epsilon(t)\rho(t)+[1-\epsilon(t)]\rho_c(t)]] = + Q_i(t)[\epsilon_i(t)\rho_i(t)+[1-\epsilon_i(t)]\rho_c(t)] - Q_f(t)[\epsilon_f(t)\rho(t)+[1-\epsilon_f(t)]\rho_c(t)] - Q_p(t)[\epsilon_p(t)\rho(t)+[1-\epsilon_p(t)]\rho_c(t)] + Q_r(t)\rho_r(t) - Q_v(t)\rho_v(t), \quad \text{(A7)}$$

where Q_v is the vapor flow and ρ and ρ_i are the density of mother liquor in the crystallizer volume and the feed flow, respectively.

Heat balance. The heat balance of the crystallizer is given by the equation:

$$\frac{d}{dt}[V(t)T(t)[\epsilon(t)\rho(t)c_{pl}(t)+[1-\epsilon(t)]\rho_c(t)c_{pc}(t)]] = + Q_i(t)[\epsilon_i(t)\rho_i(t)c_{pi}(t)+[1-\epsilon_i(t)]\rho_c(t)c_{pc}(t)]T_i(t) - Q_f(t)[\epsilon_f(t)\rho(t)c_{pl}(t)+[1-\epsilon_f(t)]\rho_c(t)c_{pc}(t)]T(t) - Q_p(t)[\epsilon_p(t)\rho(t)c_{pl}(t)+[1-\epsilon_p(t)]\rho_c(t)c_{pc}(t)]T(t) + Q_r(t)\rho_r(t)c_{pr}(t)T_r(t) - Q_v(t)\rho_v H_v + P_{\text{imp}}(t) + P_{hc}(t) + P_{\text{cryst}}(t) - P_{\text{loss}}(t), \quad \text{(A8)}$$

where T and T_i are, respectively, the temperature in the crystallizer volume and the feed flow, P_{in} is the heat supplied at the internal heat exchanger, H_v is the specific enthalpy of vapor, c_{pc} and c_{pl} are the specific heat of crystals and mother liquor, respectively, P_{cryst} is the heat of crystallization, P_{loss} is the heat loss to the surrounding, and P_{imp} is the heat supplied by pumps and stirrers.

Equations that relate the density, specific heat, and the heat of crystallization to the temperature and the concentration depend on a substance system that is crystallized and can be obtained from handbooks.

Fines dissolver. Assuming negligible holdup or delay in the fines removal section, the following two mass balances and heat balance are used to describe the ideal fines dissolver:

$$Q_r(t)\rho_r(t) = Q_f(t)[\epsilon_f(t)\rho(t)+[1-\epsilon_f(t)]\rho_c(t)], \quad \text{(A9)}$$

$$Q_r(t)C_r(t) = Q_f(t)[C(t)\epsilon_f(t)+\rho_c(t)[1-\epsilon_f(t)]]. \quad \text{(A10)}$$

The heat balance for the fines dissolver is given by

$$P_{\text{ex}}(t) = Q_f(t)\xi(t)[T_r(t)-T(t)]. \quad \text{(A11)}$$

where T_r is the temperature of the returned fines and ξ is a constant factor that is an estimated value of the specific heat of the fines flow.

Manuscript received Dec. 16, 1993, and revision received Apr. 11, 1994.